Nonlinear non-collinear ultrasonic detection and characterisation of kissing bonds

Jonathan Alston[a], Anthony Croxford[b], Jack Potter[b], Philippe Blanloeuil[c]

[a] *ACCIS, University of Bristol, University Walk, Bristol, UK +44 117 33 15311*
[b] *UNDT, University of Bristol, University Walk, Bristol, UK*
[c] *University of New South Wales, Sydney, NSW 2052, Australia*

Abstract

The development of cost effective and reliable bonded structures ideally requires an NDT method to detect the presence of poor quality, weak bonds or kissing bonds. If these bonds are more compliant in tension than in compression stress-strain nonlinearities provide a possible route to detection with the use of nonlinear ultrasonic techniques. This paper focuses on the kissing bond case and the resulting contact acoustic nonlinearity of the interface. A kissing bond is created by compression loading of two aluminium blocks. Non-collinear mixing of two shear waves producing a sum frequency longitudinal wave is the method of stimulation of contact acoustic nonlinearity in this research. The parametric space of the nonlinear mixing is measured in terms of interaction angle of the input beams and the ratio of their frequencies creating a 'fingerprint' of the sample's bulk and interface properties in the region where the beams overlap. The scattering fingerprint of a classically nonlinear solid is modelled analytically and a kissing interface is modelled numerically; these results are compared with experimentally measured values. The experimental interface is tested with varied interfacial loading, resulting in an increase in scattering amplitude as load is increased. Secondary peaks in the parameter space also appeared as loading increased, as well as other changes in the fingerprint pattern.

Keywords: Ultrasonic, kissing bond, NDT, NDE, nonlinear, non-collinear, CAN

---

1. Introduction

Kissing bonds, two surfaces in intimate contact but not bonded together, can be difficult to detect with the non-destructive testing (NDT) techniques that are standard in industry today (1; 2). For this reason, some structures are over-engineered to allow for the safe failure of an adhesive joint; 'chicken rivets' in aeronautical structures are an example of this. Kissing bonds are hard to detect with conventional ultrasound techniques because the kissing interface has a transmission coefficient very similar to the properly bonded case. This is particularly true when the interface is under compressive load. If enough acoustic stress can be applied to the interface the kissing bond will open during the tensile part of the wave. This opening and closing of the interface causes contact acoustic nonlinearity (CAN), clipping parts of the waveforms and transferring energy into other harmonics (3; 4). The research presented here aims to investigate this CAN behaviour in order to create a method for reliable, spatially sensitive, detection of kissing bonds.

There are many possible ways to detect the acoustic nonlinearity of a kissing bond. Measuring the change in transmission/reflection of the fundamental frequency is the simplest but it is insensitive due to the small changes involved (4; 5). Detecting the harmonics produced is more sensitive (1) but the harmonics often have other potential sources such as the amplifiers, transducers, couplant or the bulk materials themselves (6; 7). To overcome these problems a more advanced technique is required such as non-collinear mixing, pioneered by Jones and Kobett, and Rollins (8; 9; 10) in the 1960s. In non-collinear mixing two beams follow different paths that overlap in an area of interest. In this overlap region nonlinearities can cause the two waves to interact with each other producing a new one. The scattered beam travels in a different direction from the input beams separating its signal from the system harmonics present in the input beams that might otherwise obscure it. This creates a method which is spatially selective and when combined with filtration techniques makes it highly sensitive.

One of the conditions that must be met for bulk nonlinear mixing to occur is that the geometry of the input beams' interference pattern is such that the spacing of the antinodes is the same as the wavelength corresponding to the sum or difference of the input frequencies. The two key parameters that control the geometry of the interference pattern are the angle at which the two beams overlap (referred to as interaction angle) and the ratio of their frequencies. The optimal conditions were defined as 'resonant conditions' in (8).

Within the volume of interaction there are two main sources of nonlinearity; the classical nonlinearity of the solids (11), corresponding to the intrinsic bulk nonlinearity, which allows for the mixing of the two input beams as described by (8; 9), and the CAN. CAN generates a signal from the kissing bond in the non-collinear case by the combined acoustic forces of the two input waves opening, closing, or unloading the interface enough to allow them to slip when it would be in a different state if only a single wave were applied.

This modulation generates harmonics in a similar way to the single beam case. These perturbations effectively create an array of acoustic sources on the interface which together produce plane waves. Another difference between bulk and CAN mixing is that the latter produces scattered beams in both directions from the interface (12; 13). This can be thought of as being caused by the reflection from the interface when the two overlapping waves open it when it would be closed in the single beam case. This effect was not exploited in the following research due to difficulties in positioning an array between the input transducers but the results from transmission testing should be informative of likely reflective behaviour which would be useful for developing a one-sided NDT inspection tool.

Non-collinear mixing has been used to investigate the state of many different materials including; physical ageing of thermoplastics (14), epoxy curing (14), fatigue in aluminium (15), and oxidative aging of asphalt (16). Research into the behaviour of kissing bonds with non-collinear ultrasonic mixing is limited. Demčenko et al. conducted testing on PVC plates (17), and there has been modelling conducted by Blanloeuil et al. (13), and Zhang et al. (18). The modelling by Zhang et al. focuses on an infinite interface with nonlinear stiffness terms in one case, and a thin region region of hyperelastic solid in another case. These differ from the work presented here as their interfaces never open but the results are similar in many ways. In Demčenko's work the interaction between shear and longitudinal beams overlapping at a kissing bond at fixed angles is investigated. If the interface is defined as the x-z plane then the input beams were tested with interaction planes of x-z and y-z. When operating in the y-z plane the beams approached the interface from opposite sides. The study showed that the interface led to a reduction in nonlinear wave signal in both interaction planes. In the work presented here the input beams are in the y-z plane but both approach the interface from the same side.

Current methods consider the response for single values of interaction angle, ϕ, and frequency ratio, a, usually selected to satisfy the resonance criteria. The scattered wave amplitude however may be evaluated for a range of these parameter values, producing a surface within the a-ϕ parameter space. There is more information about the material contained within the full parameter space than can be recovered from a single experimental operating point. For classical nonlinearity, this parameter space has a characteristic shape, governed by the resonant phasing-matching condition. It has previously been observed by Blanloeuil et al. (13) in a numerical study that production of a sum-frequency wave from shear-shear mixing is also predicted by a contact-acoustic nonlinearity.

The hypothesis examined in this work is that CAN will produce a response within the wave mixing parameter space that is characteristically different from that produced by classical nonlinear terms and that, consequently, analysis of the full parameter space allows the underlying nonlinear mechanics to be identified in addition to the magnitude of nonlinearity. Further, by evaluating elastic nonlinearity using the shape of this surface, the measurements become much less sensitive to incident wave amplitude. This offers the potential for more experimentally robust nonlinear measurements. Herein the shape of the parameter-space response shall be referred to as the 'fingerprint' of the nonlinear interaction.

This study first identifies, through numerical modelling, the expected fingerprints for the shear-shear to longitudinal interaction for the cases of classical and contact-acoustic nonlinearity. An experimental program is then undertaken to acquire fingerprints for wave interactions within both bulk material and at an interface. Good agreement is found between theoretical and experimental fingerprints. The fingerprints of the classical and contact-acoustic interactions are found to be characteristically different in shape, supporting the hypothesis that the fingerprint is a useful tool for the detection of kissing bonds and, more generally, the characterisation of nonlinearity.

2. Experimental Method

To investigate the parameter space efficiently a computer-controlled, motorised rig was developed. The angle of each transducer is independently set, their lateral separation can also be controlled, allowing a constant interaction depth to be maintained with varying interaction angle. This is shown schematically in Figure 1 (a). The sample was mounted below the transducers, with an ultrasonic phased array below it in contact with its bottom surface. An array was used because as the frequency ratio is changed so is the scattering angle of the produced beam. The scattering angle for bulk mixing can be predicted by using the relevant equation from Table 1 of (8). The 40 mm length of the array was enough to capture the signal of interest in nearly all cases within the desired parameter space. The assembly was placed in a water tank, submerging the input transducers, sample, and array to minimise the coupling variation. The temperature of the water was controlled with 0.1°C precision to maintain a constant speed of sound in wa-

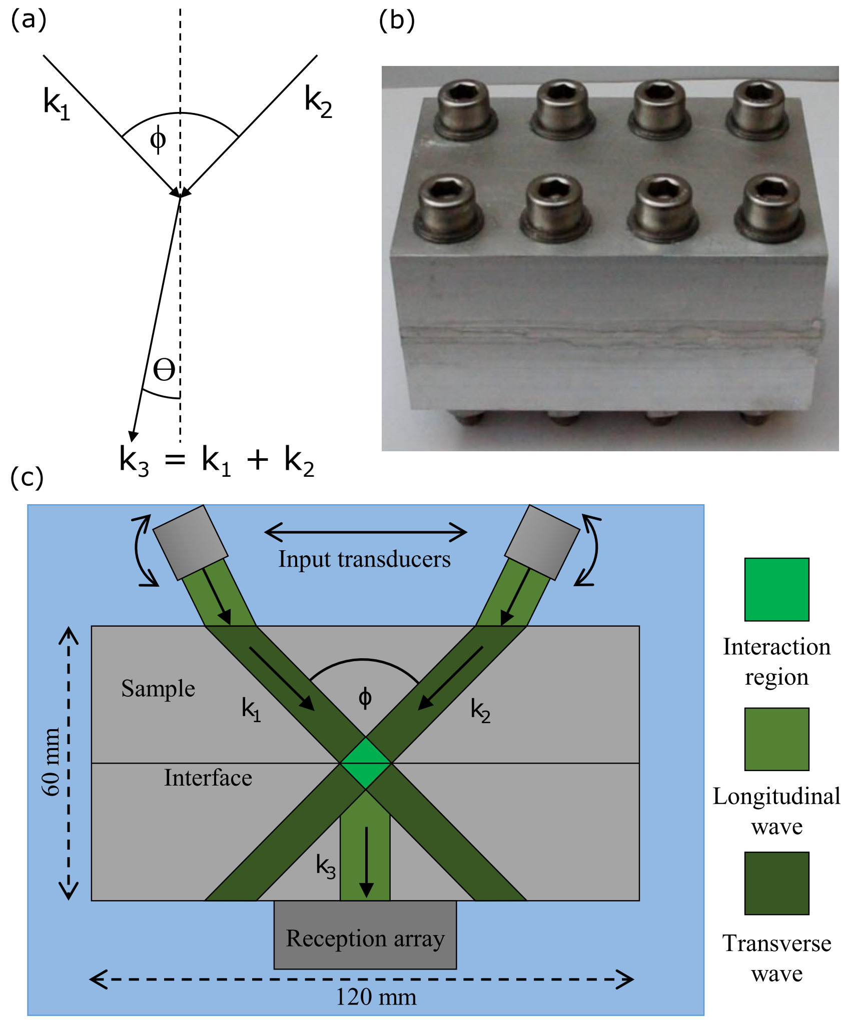

Figure 1: (a) General interaction geometry of non-collinear mixing, ϕ is the interaction angle and θ is the scattering angle. (b) Photograph of bolted aluminium sample used to simulate a kissing bond. There is sealant around the loaded interface to prevent the ingress of water. (c) Scale diagram of the experimental layout, showing simplified ultrasonic beam paths and wave types. The test is conducted in immersion.

ter, ensuring reliable refraction angles into the sample. The input pulses were generated using Agilent 33250A arbitrary waveform generators and amplified with Amplifier Research 75A250A/100A400 amplifiers. The input transducers were Olympus V551-SM's which have an active diameter of 10 mm, a peak frequency of 4.7 MHz, and a -6 dB bandwidth of 3.4 MHz. In the testing one transducer was always used at 5 MHz, and the other was varied between 3 MHz and 7.5 MHz. This results in the frequency ratio being coupled with the average input frequency which could have an additional impact on the measured fingerprints. In future work it might be better to avoid this coupling by changing both the input frequencies in order to keep a constant output. To detect the nonlinear signal an Imasonic 10 MHz linear array with a -6 dB bandwidth of 9 MHz was used. This array had 128 elements at a pitch of 0.3 mm, and was used in conjunction with a MicroPulseFMC array controller. These wide bandwidth transducers allowed frequency ratios between 0.6 and 1.5 to be tested with enough sensitivity to detect scattering even at the extremes.

Absolute interaction angle accuracy is approximately $\pm 2°$. Most of this error is systematic, the random error has a standard deviation of only $0.2°$. This means that very similar parameter spaces are sampled every time, giving reliable comparison between fingerprints, but single points in the space may have up to $2°$ error in absolute terms.

The samples discussed in this report were both 2024 T351 aluminium blocks with outer dimensions of 120 x 80 x 60 mm. A solid block was used as a reference and another block cut into two halves and compressively loaded together with bolts to simulate a kissing bond. The reference block allows measurements of just the bulk nonlinear behaviour. The interface testing was conducted with the contacting surfaces finely ground using P1000 grit wet and dry paper (18 micron average particle size). Different results would be expected with different surface finishes due to changes in the fraction of the surfaces in contact and the range of angles at which they meet, although this is not tested in this work. The torque on the bolts of the two-part block was varied, using a torque wrench, altering the loading on the interface, see Figure 1 (b). The use of bolts along the sides allows unobstructed ultrasonic access to a large section of the block, this gives greater flexibility in the measurements that can be made when compared to the conventional universal testing machine method of loading. The main negative of the technique was the random error in loading magnitude due to the unreliable frictional behaviour of the nuts/bolts and the systematic error due to the difficulty in directly measuring the applied load. Another limitation was the loading range due to the 5 to 50 Nm torque range. Lower torques than this were very inaccurate due to frictional effects, and larger torques would be hard to apply manually. The interface sample was sealed with silicone to prevent water ingress when immersed. FE modelling, in Abaqus, was conducted to verify that the dimensions of the blocks and bolts should give an even interface loading along the centre. This modelling predicted that a torque of 5 Nm should produce a compressive load of 2 MPa in the region of inspection, however due to the experimental samples not being perfectly flat there is likely to be some error in this.

It should be noted that the approximation of a kissing bond by the compressive loading of the two plates is not intended to produce an interface that is undetectable to conventional linear methods. The focus here is on measuring the CAN mixing behaviour in a simplified scenario so that the knowledge can then be applied to the detection of more realistic invisible kissing bonds in later research.

There are many modes of non-collinear mixing possible (8), investigated in this work is the interaction of two shear waves producing a longitudinal wave at the sum of the two incident frequencies. This mode was used mainly due to the simplicity of producing exclusively shear waves over a wide range of angles, and because it allows for the generation of mixing from both the bulk nonlinearities and CAN which enables the bulk signal to be used as a reference for the CAN signal amplitude. If the aim of the experiment were to avoid the production of bulk scattering and only produce CAN scattering a different interaction mode, such as the mixing of two longitudinal waves, would be preferred. 20-cycle Hann-windowed pulses were used for both input transducers. These long pulses create a narrow frequency bandwidth which makes the experiment more sensitive to frequency ratio and improves the filtering of the output signal because the energy is within a smaller frequency window. The Hann window is used to reduce frequency sidebands. For each combination of interaction angle and frequency ratio three measurements were taken; signal with both transducers emitting, signal with just the left transducer, and signal with just the right. The signals received from the left and right were subtracted from the case where both were emitting simultaneously (Figure 2 shows examples of the time data at various points of acquisition and processing). In plots a, b, and c of Figure 2 the side lobes of the input pulses dominate but after subtraction, shown in plot d, the scattered pulse becomes visible. Note the different colour scales. Filtering at the sum frequency, Figure 2 (e), removes nearly all of the remaining unwanted signal allowing the pulse of interest and its echoes to be clearly seen.

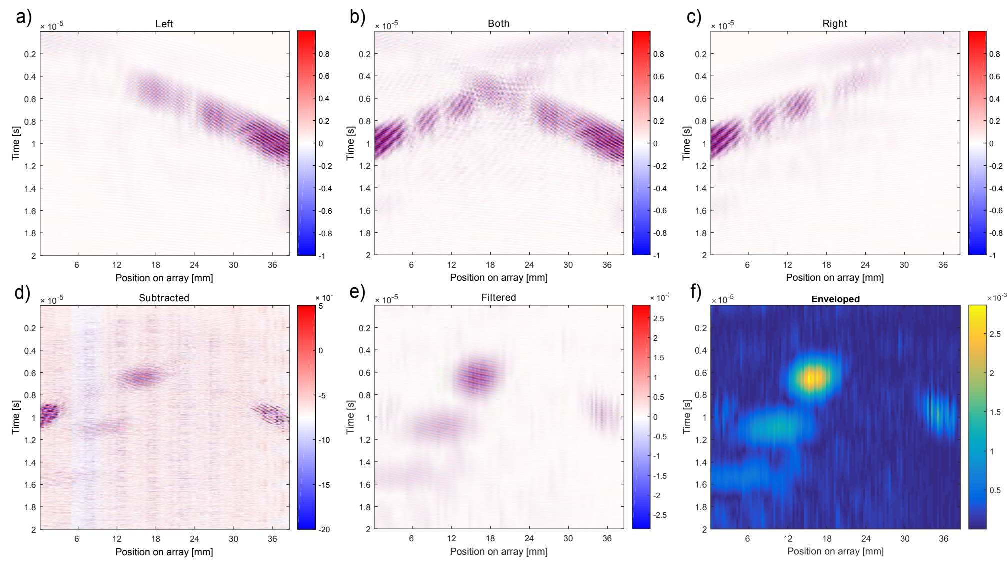

Figure 2: Time data captured by the array shown at various stages of processing. Array element position is on the x-axis and time in seconds on the y-axis. Note the differing colour scales. The data was collected for a frequency ratio of 0.8 and an interaction angle of 120° in solid aluminium. (a) The raw signal received when the left transducer is fired at ω_1 (5 MHz), (c) is the right at ω_2 (4 MHz) and (b) is both at their respective frequencies. The result of subtracting left and right from both is displayed in (d). (e) The subtracted signal after filtration at the mixing frequency $\omega_1+\omega_2$ (9 MHz). The envelope of the signal is shown in (f).

Pulse inversion is a commonly used technique in nonlinear ultrasonics (19; 20; 21) as it can be used to remove either the even or odd harmonics from the signal. However, it is less useful in sum-frequency non-collinear mixing since the signal of interest is at a similar frequency to the second harmonic of the input beams when the frequency ratio is close to one. In non-collinear mixing the second harmonic component of the input beams' side lobes is commonly the largest source of unwanted signal that remains after processing in the way detailed in the previous paragraph. Conventional pulse inversion is not able to remove these side lobes while enhancing the sum-frequency scattered wave. There is a more advanced form of pulse inversion where all combinations of inversions of the input pulse are applied, requiring a total of four firings (22). This method was not used in the experimentation presented here but it looks very promising for future work.

A window of the data in time and space was selected based upon the predicted time of arrival and angle of scattering, as stated in (8). This window removed most of the unwanted signal from the sidelobes of the input beams that normally arrived later than the signal of interest. Focusing on reception was then performed to enhance the measurement of the wave scattered by the interface. To do so a delay is applied to each element's response, depending on the position of the element within the array and its location with respect to the interaction volume. The remaining signal was then summed element-wise to complete the focusing operation. Finally, the Hilbert transform was used to acquire the envelope of the signal and the peak value of this was recorded. This value is used as the metric of scattering and referred to in later figures as 'peak scattering amplitude'. By recording this scattering value for the range of input parameters a 'fingerprint' can be made. These steps are shown as a flowchart in Figure 3.

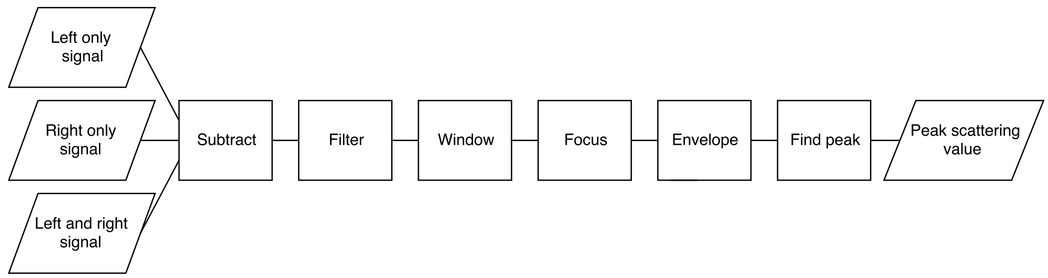

Figure 3: The steps involved in the processing the three captured time signals into the value used for one point in the fingerprint. The steps are described in detail in the main text.

3. Modelling

A program of numerical modelling was undertaken in order to determine the independent contribution of both the classical and contact acoustic nonlinearity on the wave mixing parameter space. The modelling is also useful to inform which areas of the parameter space are likely to be of interest so that the experiment can be designed to include these ranges.

Knowledge of the experimental geometry, apparatus, and processing techniques is used in the production of models that more accurately relate to the experimental measurements. Many factors such as transducer bandwidth, mode conversion at the water-aluminium interface, and interaction volume have significant impacts on the resulting fingerprints so are included in the following results.

3.1. Classical nonlinear solid

The classical nonlinearities of the bulk material can be modelled by the extension of 3rd order elastic energy equations derived in (8) and (9) to off-resonance conditions. The equation for the particle displacements of the scattered longitudinal wave at the sum frequency of the input waves is given by (8) in Equation 1.

$$\mathbf{u_s}(\mathbf{r},t) = \frac{(\mathbf{I}\cdot\hat{r})}{4\pi c_l^2\rho_0}\int_V \sin\left[\left(\frac{\omega_1+\omega_2}{c_l}\hat{r}-\mathbf{k_1}-\mathbf{k_2}\right)\cdot\mathbf{r'}-(\omega_1+\omega_2)\left(\frac{r}{c_l}-t\right)\right]\mathrm{d}V \tag{1}$$

Where $\mathbf{r}$ is position vector of the observation point relative to the centre of interaction, $\hat{r}$ is a unit vector in the direction of $\mathbf{r}$, $\mathbf{r'}$ is the position vector of an interaction point relative to interaction volume centre (a figure of these vectors is presented in (8)), t is time, c_l is the longitudinal velocity, ρ_0 is the material density, V is the interaction volume, $\mathbf{k_1}$ and $\mathbf{k_2}$ are the input wave vectors, ω_1 and ω_2 are the corresponding angular frequencies, and $\mathbf{I}$ is an interaction parameter given by the following Equation 2.

$$\begin{aligned}
\mathbf{I} = &-\frac{1}{2}(\mu+\frac{1}{4}A)\,[\,(\mathbf{A_0}\cdot\mathbf{B_0})(\mathbf{k_2}\cdot\mathbf{k_2})\mathbf{k_1}+(\mathbf{A_0}\cdot\mathbf{B_0})(\mathbf{k_1}\cdot\mathbf{k_1})\mathbf{k_2}\\
&+(\mathbf{B_0}\cdot\mathbf{k_1})(\mathbf{k_2}\cdot\mathbf{k_2})\mathbf{A_0}+(\mathbf{A_0}\cdot\mathbf{k_2})(\mathbf{k_1}\cdot\mathbf{k_1})\mathbf{B_0}\\
&+2(\mathbf{A_0}\cdot\mathbf{k_2})(\mathbf{k_1}\cdot\mathbf{k_2})\mathbf{B_0}+2(\mathbf{B_0}\cdot\mathbf{k_1})(\mathbf{k_1}\cdot\mathbf{k_2})\mathbf{A_0}\,]\\
&-\frac{1}{2}(K+\frac{1}{3}\mu+\frac{1}{4}A+B)\,[\,(\mathbf{A_0}\cdot\mathbf{B_0})(\mathbf{k_1}\cdot\mathbf{k_2})\mathbf{k_2}+(\mathbf{A_0}\cdot\mathbf{B_0})(\mathbf{k_1}\cdot\mathbf{k_2})\mathbf{k_1}\\
&+(\mathbf{B_0}\cdot\mathbf{k_2})(\mathbf{k_1}\cdot\mathbf{k_2})\mathbf{A_0}+(\mathbf{A_0}\cdot\mathbf{k_1})(\mathbf{k_1}\cdot\mathbf{k_2})\mathbf{B_0}\,]\\
&-\frac{1}{2}(\frac{1}{4}A+B)\,[\,(\mathbf{A_0}\cdot\mathbf{k_2})(\mathbf{B_0}\cdot\mathbf{k_2})\mathbf{k_1}+(\mathbf{A_0}\cdot\mathbf{k_1})(\mathbf{B_0}\cdot\mathbf{k_1})\mathbf{k_2}\\
&+(\mathbf{A_0}\cdot\mathbf{k_2})(\mathbf{B_0}\cdot\mathbf{k_1})\mathbf{k_2}+(\mathbf{A_0}\cdot\mathbf{k_2})(\mathbf{B_0}\cdot\mathbf{k_1})\mathbf{k_1}\,]\\
&-\frac{1}{2}(B+2C)\,[(\mathbf{A_0}\cdot\mathbf{k_1})(\mathbf{B_0}\cdot\mathbf{k_2})\mathbf{k_2}+(\mathbf{A_0}\cdot\mathbf{k_1})(\mathbf{B_0}\cdot\mathbf{k_2})\mathbf{k_1}]
\end{aligned} \tag{2}$$

Where K and μ are the compression and shear moduli respectively, A, B, and C are the third order elastic constants, and $\mathbf{A_0}$ and $\mathbf{B_0}$ are the input wave amplitude vectors that point in the direction of polarisation. From these equations the interaction angle that produces maximal scattering for a given frequency ratio was derived in (8) for each interaction case. For the interaction of two shear waves producing a sum-frequency longitudinal wave the 'resonance' equation is

$$cos\phi = c^2 + \left(\frac{(c^2 - 1)(a^2 + 1)}{2a} \right) \tag{3}$$

where ϕ is the interaction angle, c is the velocity ratio between transverse and longitudinal waves c_t/c_l, and a is the frequency ratio ω_1/ω_2. The resonant conditions predicted by this equation are plotted on all fingerprints in this report for reference. This is useful for predicting the parameters that produce maximal mixing but to predict the mixing response over the full parameter space Equations 2 and 1 were numerically solved. This can be done for an arbitrary interaction volume but by simplification to a cylindrical volume with a uniform intensity profile an analytic solution can be found, increasing the speed of the model. These assumptions limit the accuracy but provide a way to quickly estimate classical nonlinearity's influence on the fingerprint.

By calculating the scattering amplitude over a range of interaction angles and frequency ratios the fingerprint of the classical nonlinearity can be produced, Figure 4. For this modelling a radius of 17.5 mm was used for the interaction volume and the properties of the aluminium were; Young's modulus $E = 73.1$ GPa, Poisson coefficient $\nu = 0.33$, density $\rho = 2780$ kg.m^{-3}, and Murnaghan coefficient $m = -397$ GPa. The other third order elastic coefficients (TOECs) are not required since they cancel out for the interaction of two horizontally polarised shear waves forming a longitudinal. It was found that the shape of the parametric response was insensitive to changes of about a factor of two in m so although there is significant variation in the literature values (23; 24) a similar fingerprint would be expected from most aluminium samples. The model was run with the frequency of one of the input beams fixed at 5 MHz.

Correction factors were applied to the result to account for experimental factors not within the scope of the model to allow the results to be compared with later experimental measurements more accurately. The bandwidth of the input transducers and detection array was modelled as Gaussian with the values stated in Section 2. Mode conversion at the water-aluminium interface was accounted for with the equations stated in (25). Angular sensitivity of the experimental array due to the pitch of its elements was calculated using the directivity function, D, and applied based upon the predicted scattering angle

$$D(\theta) = \mathrm{sinc}\left(\frac{\pi a \sin\theta}{\lambda}\right) \tag{4}$$

where θ is the angle to the normal of the array, a the pitch, and λ the wavelength of the scattered wave.

It can be seen in Figure 4 that the strongest mixing response is predicted at 118° and a frequency ratio of 1.06. This is approximately the same angle as the resonance angle given by the equation stated in (9), 120°. There are also two secondary lobes of nonlinear scattering that can be seen at smaller interaction angles, peaking at around 100° and 85°. The reduction in amplitude at frequency ratios far from 1 is due mainly to the bandwidth of the transducers, and the cut off at angles smaller than 60° is caused by

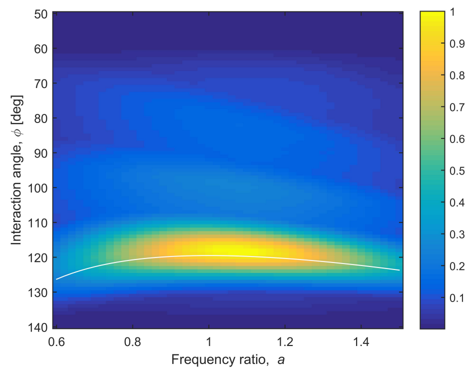

Figure 4: Analytic modelling of parametric space of mixing in solid aluminium. Adjusted to include experimental factors. Arbitrary colour scale indicates scattering amplitude. White line indicates the resonant conditions.

very little production of shear waves at the water/aluminium interface below the first critical angle. These results predict that there are multiple features in the fingerprint within the 60° to 140° that might interfere with the CAN signals of interest presented in the following section.

3.2. CAN finite element model

The nonlinearity of the kissing interface is very different from the classical bulk nonlinearity, as such it is not obvious based upon previously established theory that the interface would cause two incident shear waves to interact to produce a scattered longitudinal wave. The modelling conducted in this section shows that a kissing interface can cause non-collinear mixing, as others have done previously, and it explores the parametric sensitivity of the mixing.

The behaviour of a contacting interface requires a model that can accurately capture how the interface can be in one of three states, strongly closed

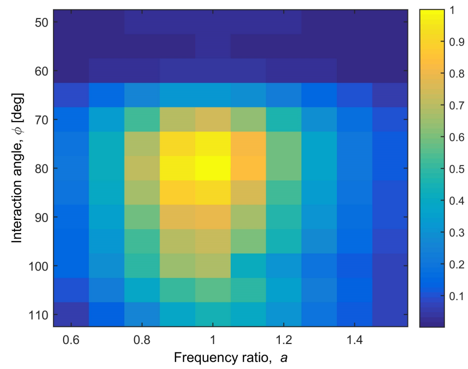

Figure 5: FE modelling of parametric mixing response of aluminium-aluminium kissing interface. Adjusted to include experimental factors. Arbitrary colour scale indicates scattering amplitude.

(transferring transverse and normal stresses), slipping (transferring only normal stress), and open. This was achieved using a 2D plane strain FE model. The model is similar to the one reported in (13), with differences in terms of geometry and incident frequencies. The main characteristics of the FE model are detailed below for completeness. This model does not include the higher order elastic terms so classical bulk mixing should not occur.

The two contacting aluminium blocks were 120 $\times$ 30 mm and modelled as homogeneous and isotropic solids, with Young's modulus $E = 69$ GPa, Poisson coefficient $\nu = 0.33$ and density $\rho = 2700$ kg.m^{-3}. Clamped boundary conditions were imposed on both left and right faces of the blocks to prevent any body motion, while input excitations were imposed on the top face of the assembly and output displacements were recorded at the bottom face. More precisely, two incident shear waves were generated from the top face by imposing nodal displacement along the x-axis over 10 mm long segments, and appropriate time-delays were used to generate the waves with the desired angle of incidence. Additionally, the spacing between the excitation sources was always chosen to ensure intersection of the incident beams at the contact interface. The angle between the incident beams was varied from 50° to 110° in 5° steps. The left shear wave had a fixed frequency of 2 MHz, whereas the right shear wave had a frequency between 1.2 MHz and 3 MHz giving frequency ratios between 0.6 and 1.5 in increments of 0.1. A centre frequency around 2 MHz was used in the FE model instead of the 5 MHz used experimentally to maintain reasonable computation time, since high frequencies impose small element dimensions and thus larger computation time. Both incident shear waves were 8-cycle sinusoidal Hann-windowed tone bursts regardless of the excitation frequency. Note that when varying the frequency of the right source, the angle between the incident beams was kept fixed. If CAN is activated, a longitudinal wave is expected to propagate toward the bottom face. Displacements were recorded along the bottom face and post-processed in the same way as experimental signals, as detailed in Section 2. Measurements could also have been taken from the top surface but the aim was to mimic the experimental method as closely as possible. Previous work by Blanloeuil et al. showed this modelling technique predicts a backwards propagating scattered wave (13).

Modelling of the contact interface between the two solids must account for CAN. In the FE model, a unilateral contact law with Coulomb's friction was considered between the two solids, with a coefficient of friction $\mu = 0.5$. Thus, three states can be observed simultaneously at different locations along the interface: open interface, frictional sliding contact and closed interface.

Moreover, a static compression stress $\sigma_0 = -0.05$ MPa was introduced in the definition of the contact laws to account for external compression of the system. The contact laws are defined in (13) and represent a simplified model of the contact interface that captures the essential contribution of contact dynamics to the scattering response as done previously in (13; 19; 26).

The FE model was obtained from the discretisation of this geometry and the resolution was done using the 2D FE code Plast2 (27; 28). A comparison between Plast2 and Abaqus for large deformation contact problems is presented in (29). In Plast2, the solution is evaluated in the time domain with contact algorithms formulated using the forward Lagrange multipliers method (30) which enables the use of Lagrange multipliers in a time explicit integration. More precisely, the contact equations are respectively satisfied at time t and $t + \Delta t$. To make this possible, the contact equations are solved using a Gauss-Seidel iterative solver. The global method is thus semi-implicit and the time step is subject to the Courant-Friedrichs-Lewy (CFL) stability condition $\Delta t \leq a_{min}/c$, where a_{min} corresponds to the smallest element dimension and c to the longitudinal wave velocity in the medium. The spatial discretisation is essential in the FE method. In order to have an accurate solution, the wavelength of the highest frequency component of interest should be sufficiently discretised. As the frequency of the scattered longitudinal wave is equal to the sum of incident frequency, its maximum value is thus 3.5 MHz and the corresponding wavelength is close to 1.7 mm. Therefore, a regular mesh was constructed with 0.1 mm square elements, thus ensuring a sufficient discretisation of the wavelength for both the incident shear waves and the scattered longitudinal wave. The mesh was made only of fully integrated quadrangle elements of type Q_1 (31). To satisfy the CFL stability condition for the current mesh dimensions, the time step was set to $\Delta t = 3$ ns.

The model consisted of 720000 elements, 723002 nodes (each node has two degrees of freedom) and took about 11 hours to solve for each parametric point on an average desktop PC. Since 130 different points in the parameter space were investigated over 1000 hours of computation time was required to generate the fingerprint. The code does not currently make use of parallel or GPU computing so it might be possible to reduce the time requirements by these methods in the future. Since the model used for this work is presented in other publications further details will not be shown or discussed here. The following is about the resulting fingerprint produced when the time signals from an array of points below the crack are processed in the same way as defined in the experimental methods section.

FE simulations were run for different values of interaction angle and frequency ratio in order to obtain the fingerprint of the nonlinear response resulting from the non-collinear wave mixing, Figure 5. The FE predicts a peak in nonlinear mixing at approximately 78°. The optimum frequency ratio of the model was 1.0 but after applying the experimental centre frequency correction it was shifted to around 0.95. The mixing response is much broader in terms of interaction angle than the classical bulk mixing. This was expected since the resonance conditions do not apply to a 2D CAN source. The response pattern is thought to be due to the magnitude of normal stress exerted at the interface which peaks at an incident angle of 45° (90° interaction angle). The observed peak, however, is at a smaller interaction angle than this, possibly due to the beam sources having a shorter propagation length at smaller angles, reducing beam spread and thus increasing the amplitude of the input waves.

It can be seen that the two fingerprints (Figures 4 and 5) are easily distinguishable due to their angular responses however since they both produce signals across a wide range of interaction angles there is likely to be some interference between the two sources. If the classical mixing is much stronger than that of the CAN then detecting the presence of an interface could be difficult. It is unknown from the modelling how the two mixing sources will interfere with each other, it may be possible to subtract the bulk mixing from an experimental fingerprint to leave only the interface signature if the two act constructively. Experimental testing is required to see if this is necessary and possible. The overlap of these fingerprints in the interaction angle dimension also suggests that a measurement made at a single interaction point might produce a signal that is caused by the complex combination of the bulk and interface nonlinearity and that only measuring at multiple points in the parameter space could provide certainty. This modelling indicates that fingerprints over the range 70° to 130° be captured to include the primary features associated with each type of mixing. In order to avoid the interference between these two signals the detector could be positioned on the same side as the input transducers allowing detection of only the reflected CAN signal. This was not done in this case due to limitations in the available equipment and experimental geometry.

4. Experimental results

4.1. Solid sample

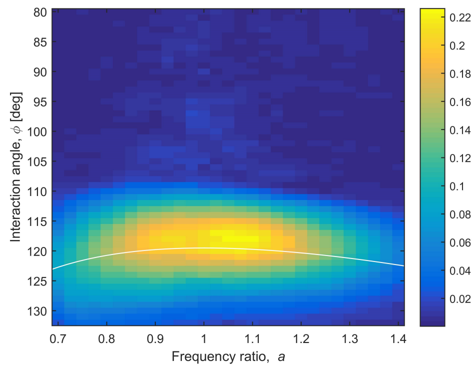

Figure 6: Experimentally measured parametric space of solid aluminium sample at a depth of 18 mm. Colour scale indicates scattered amplitude (as defined at the end of Section 2) normalised to peak of Figure 8. White line indicates the resonant conditions.

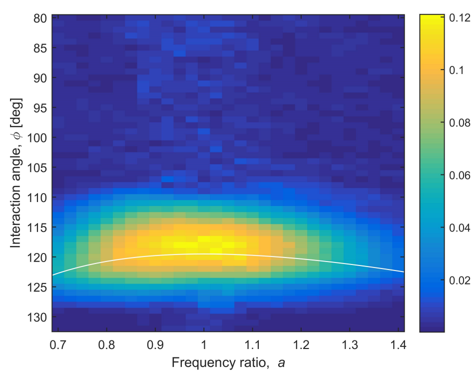

Figure 7: Experimentally measured parametric space of solid aluminium sample at a depth of 30 mm, the middle of the block. Colour scale indicates scattered amplitude normalised to peak of Figure 8. White line indicates the resonant conditions.

The modelling demonstrated the possibility of bulk mixing happening at smaller interaction angles than its resonance condition. This could potentially obscure interface mixing measurements so testing of solid material must be done first to understand its influence on later interface fingerprints. Figure 6 shows the nonlinear response of aluminium 2024 T351, with the interaction volume's centre at 18 mm below the surface of the 60 mm thick block. In this most simple case the fingerprint has only one peak, at the angle predicted by the classical equations (8; 10). Fingerprints have been taken at various input power levels and depths (10 mm to 30 mm) into the material, despite these changes the fingerprint remains largely unchanged in shape. The intensity of the pattern is proportional to the product of the input beams' amplitudes, as expected. Figure 7 shows the fingerprint of the solid aluminium at a depth of 30 mm (the centre of the sample). The fingerprint is quite similar to that taken at 18 mm, again showing only one peak in response approximately at the resonant condition. There are some slight differences between measurements at 18 mm and 30 mm however. The decrease in intensity at angles greater than 125° at 30 mm deep is due to a geometric limitation that reduces the fraction of the beams able to propagate into the sample. This is caused by the larger input beam separations required for deeper interactions. Another notable difference between the two fingerprints is their overall amplitude; at 18 mm deep the scattering response is nearly twice that at 30 mm. This is mainly due to beam divergence as they propagate through the sample, reducing beam amplitude but increasing volume of interaction. The scattering amplitude is proportional to the interaction volume and the square of the input amplitude. The combination of these two factors results in scattering amplitude being proportional to the inverse of beam radius at the interaction point.

The classical modelling predicted that there would be a primary mixing peak at 118° ranging from 110° to 130°, this matches the experimental data very well, Figure 6. It also predicted the existence of smaller peaks in mixing at angles of 100° and 85°, Figure 4, with the 100° peak having a quarter of the magnitude of the main mixing region. It does not look like these secondary peaks are present in the experimental fingerprint. There is some signal visible between 95° and 106° experimentally but it is much smaller than predicted and is likely due to poor filtration of input beam side lobes at frequency ratios close to 1. Otherwise the model and experiments agree well showing a main mixing region between 110° and 130° and similar behaviour in terms of frequency ratio.

4.2. Kissing interface

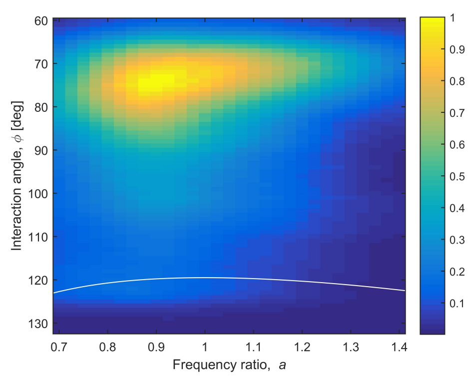

Figure 8: Experimentally measured parametric response of aluminium kissing interface sample at a depth of 30 mm, the middle of the block. Bolt torque at 40 Nm. Colour scale indicates arbitrary scattered amplitude, standardised with Figures 6 and 7. White line indicates the resonant conditions.

Now that a benchmark for solid aluminium mixing has been obtained the interface sample can be studied for comparison. Figure 8 shows a fingerprint of the compression loaded interface sample, with the volume of interaction centred on the interface. The reduction in signal seen at 125° and greater is due to the geometric limitation mentioned previously in Section 4.1. A peak in mixing behaviour is observed at around 75° and a frequency ratio of 0.9 in this case. There is a much smaller peak at around 100°, and a very slight peak at frequency ratios around 0.85 at 120°. Figures 6, 7, and 8 were normalised to the maximum scattering amplitude of the three which occurred in the interface case. The maximum scattering amplitude from the interface was an order of magnitude larger than that from the solid sample at the same depth.

FE modelling predicted a peak at 78° compared with the observed 75°. The experiment has an absolute error of $\pm 2°$ and the modelling only had a resolution of 5° so these values are within error bounds. The optimum frequency ratio of the model was 1.0 but after applying the experimental centre frequency correction it was shifted to around 0.95. This compares with the experimental peak frequency ratio of 0.90, again showing good agreement. The peak at 120° is expected as it was predicted by the classical nonlinear model and observed in the solid sample, Figures 4 and 6. The peak at 100° was predicted by the classical model but not seen in the solid experimental measurement, thus it is unlikely that this peak is due to bulk nonlinear mixing. The CAN FE model did not predict any significant secondary peaks when run at 5° interaction angle steps. This parameter space was quite coarsely sampled and might miss narrow peaks so more detailed modelling was conducted at a frequency ratio of 1.0 with smaller 2.5° interaction angle steps. Again, no peaks other than the main one at 78° were observed in this data. Later in this section fingerprints are captured at different interface loadings, some exhibit no secondary peaking so perhaps the model would also produce secondary peaks given particular interface conditions. A possible explanation for the bands is suggested later in the paper.

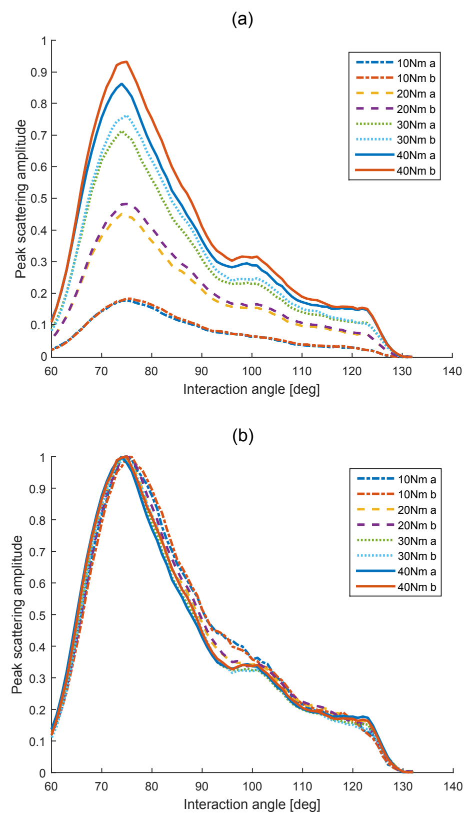

Figure 9: (a) Scattering amplitudes from aluminium compression loaded rough interface sample at a frequency ratio of 0.9 with bolt torques ranging from 10 to 40 Nm. The first loading cycle is labeled 'a', and the second 'b'. The peak scattering amplitude is an arbitrary unit relative to the maximum scattering observed in Figure 8. (b) This plot contains the same data as (a) except it has been peak normalised for each loading point.

The most useful trends in the fingerprints appear to occur in the interaction angle dimension therefore further testing was conducted at a single frequency ratio, 0.9. This was selected as it was near the peak response points of both solid and interface samples and far enough away from 1.0 that it had reduced noise from the frequency filtering.

Values for the peak scattering amplitude are presented in two ways in the following sections. In part a of the figures the values have been normalised by the peak value obtained in the kissing interface fingerprint, Figure 8. In part b the data is normalised by the peak scattering of each parametric sweep. The former is to allow for absolute amplitude trends to be compared and the latter for comparison of fingerprint shapes.

Figure 9 (a) shows the scattering response of the interface region at a frequency ratio of 0.9 with bolts torqued between 10 Nm and 40 Nm. This range was used because very little signal was observable with the torque below 10 Nm, and 40 Nm was as much as could be applied to the sample with the torque wrench. Since it is very difficult to know accurately the interface pressure with this experimental method bolt torque will be referred to as the controlled variable. The two are predicted to be directly proportional, ignoring microscopic contact changes. The sample was preloaded to 40 Nm before the two full loading cycles, 'a' and 'b', were tested. For the cycles the bolts were torqued to 10 Nm initially then increased in steps of 10 Nm up to 40 Nm. As the loading was increased the amount of mixing increased. When 10 Nm was applied the main CAN related peak is seen at around 76°, this shifted approximately 2° towards smaller interaction angles as the load increased. This plot also shows that there was an overall trend of increased scattering with each loading cycle. This can be explained by the fact that the interface was never fully unloaded during these cycles, each bolt was unloaded from 40 Nm and re-tightened to 10 Nm in turn, keeping the faces in constant contact. This method was intended to stop the faces moving relative to each other between each cycle, keeping the same parts of the interface in contact. Due to this it is expected that the surface asperities will gradually deform to match each other with each cycle, increasing the contact between the two faces and thus the transmission.

Despite the many differences in the parameter space at various loads it is notable how similar the trends are when peak normalised, as shown in Figure 9 (b). The shape produced is very different from the solid sample response demonstrating the potential of this technique to identify the presence of kissing bonds at a range of loads. There are also many subtle trends visible in this normalised data; firstly, as torque is increased from 10 Nm to 30 Nm the 100° feature becomes more pronounced, but it is unchanged when further increased to 40 Nm. Secondly, there is a notable lack of change in the relative amplitudes of scattering seen at 76° and 120°. It might be expected that these areas should respond differently to increased interface load if the former is due to CAN and the latter classical bulk nonlinearities. If it is assumed that half the interaction volume is above the interface and half below an equation for the expected bulk signal as a fraction of the solid sample's can be formed. The signal produced above the interface is reduced by a factor of T_o, the transmission coefficient at the output frequency, and the signal created below the interface would be reduced by T_i^2 due to the reduction of both input beams by the interface, thus

$$S_i = 0.5 \times (T_i^2 + T_o) \times S_s \tag{5}$$

where S_i is the predicted classical signal amplitude from the interface sample, and S_s is the signal from a solid sample. As loading is increased both the transmission coefficients would be expected to increase resulting in a monotonic relationship between loading and S_i. There is not a direct relationship predicted between transmission coefficient and CAN mixing amplitude so it would be likely to scale differently. The assumption that the signal seen at 120° is due to bulk nonlinearities is likely to be false though, as can be seen upon further analysis of Figures 7 and 8. In Figure 8 the scattering amplitude of the interface sample is 0.17 arbitrary units at 120° and frequency ratio of 0.9. This compares with 0.11 in the solid block in Figure 7 at the same frequency ratio and angle. Therefore, even if the interface were perfectly transmissive (which it is not) the scattering due to bulk nonlinearities could only account for 64% of the overall scattering produced. Therefore the interface must be responsible for a significant amount of the scattering observed at 120°.

In the paper by Blanloeuil et al. (13) the FE modelling predicted that the maximal mixing response occurs when the interface load is 0.25 that of the peak combined acoustic loading. The experimental acoustic loading was estimated by using a laser vibrometer. A measurement was taken with one of the input beams at normal incidence on a 30 mm thick aluminium sample. The surface deflection due to the longitudinal wave that propagated through the sample was converted into an acoustic stress. Using mode conversion calculations an estimate was made of the combined acoustic stress of two shear waves in the aluminium that would be created when an interaction angle of about 80° is used. The resulting value was 0.1 MPa, but due to the many approximations involved this is probably only accurate to an order of magnitude. Using this value of acoustic stress gives an expected peak response at 0.025 MPa interface loading which corresponds to bolts torqued to 0.05 Nm. This is much smaller than the experimentally tested range of 10 - 40 Nm in which the mixing was observed increasing with load. The laser vibrometer measurement and torque to interface pressure estimations were quite rough but a disagreement of at least three orders of magnitude suggest that there is likely another source of difference between the model and experimental measurements. One possible difference is the smoothness of the interface with the modelling being perfectly flat and having completely evenly distributed loading.

4.2.1. Repeatability

To demonstrate the repeatability of the method a plot of measurements taken at 40 Nm torque is shown in Figure 10. It contains a parametric sweep taken after the plates were first loaded to 40 Nm (the pretest measurement), another taken after the load was released and then reapplied on each bolt in turn (a), and two after a second load cycle (b). The sample was removed from the immersion tank and replaced between the two 'b' tests. It can be seen in Figure 10 (a) that the pretest measurement had amplitudes 25% smaller than the cycles that followed, and that there was about a 10% variation in amplitudes of cycles a and b. The variation in amplitude with cycle number is expected as surface asperities are altered by each successive cycle, although most of the deformation occurs during the first (4). Initially the

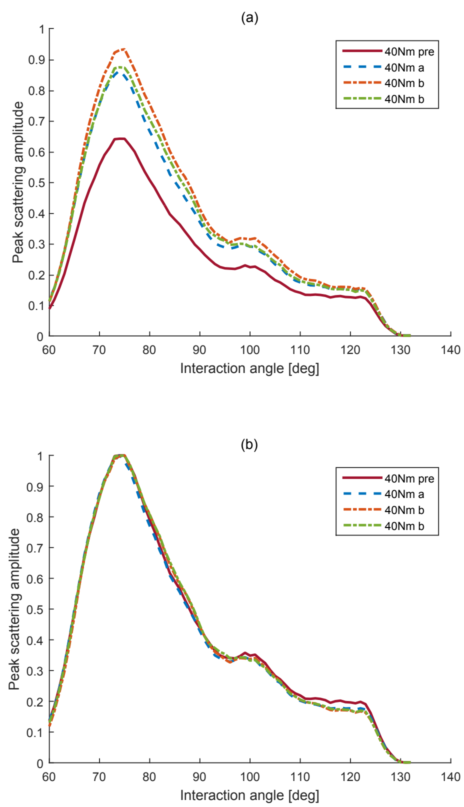

Figure 10: Scattering amplitudes at a frequency ratio of 0.9 for the rough interface sample. (a) The measurements at 40 Nm torque are shown from the pretest cycle, cycle 'a', and two cycle 'b' tests. The peak scattering amplitude is an arbitrary unit relative to the maximum scattering observed in Figure 8. (b) This plot contains the same data as (a) except it has been peak normalised for each loading point.

surfaces only contact where they are locally raised. Due to the small area in contact this area is under high load and unable to be overcome by the acoustic stress. The remaining troughs are not in contact so transmit no signal. The combination of these factors leads to small CAN signals when the plates are first brought together but cause the signal to increase as the surfaces conform to each other. This process is expected to be more dominant in a roughly ground interface case than for a polished interface because the asperities of the polished interface should be much smaller and form a better match initially.

The normalised data in Figure 10 (b) displays very good agreement between the measurements, only the pretest response significantly differed from the others, having a smaller 120° to main peak ratio. Some difference would be expected due to the changing interface condition discussed above. This data gives an indication of the repeatability of the measurement, showing that peak normalisation results in consistent parametric trends when the sample is unaltered. Measurements taken consecutively without the removal of the sample were conducted, these showed even smaller variation than seen above, leading to the conclusion that positioning of the sample is the primary cause of the slight variation observed in '40Nm b' trends in Figure 10 (b). The impact of positioning is explored in the following section.

4.3. Position sensitivity

There is almost certainly some variation in the average surface height of the blocks between points a few millimeters apart due to the limitations of the production method used, therefore it is expected that some macroscopic regions of the interface will be under greater average load than others despite

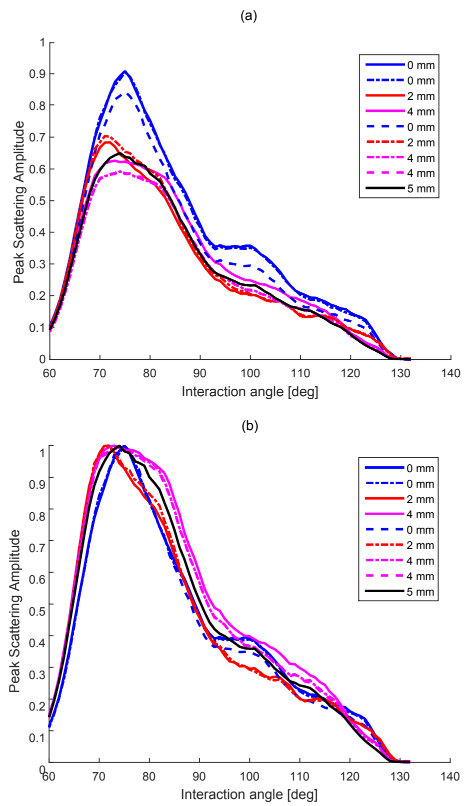

Figure 11: Scattering amplitudes at 0.9 frequency ratio of rough aluminium interface loaded by bolts at 40 Nm. Tests were conducted with the sample in four different positions, with 0 mm displacement being the same position as used for previous interface tests. The legend indicates the order in which the measurements were taken. The peak scattering amplitude is an arbitrary unit relative to the maximum scattering observed in Figure 8. (b) This plot contains the same data as (a) except it has been peak normalised for each position point.

efforts to design a geometry that minimises loading variability. Due to this it might be expected that testing a different region of the interface could yield a fingerprint that resembles another taken at a different torque setting. To investigate this the interface sample had scattering measurements taken at various points along the central axis of the sample, specifically at 0, 2, 4, and 5 mm from the centre. In Figure 11 (a) the unadjusted arbitrary amplitudes can be seen. The bolt torque was 40 Nm for this testing. The reduction in signal observed at above 120° for increasing displacements is related to the input beam clipping issue mentioned previously.

At all measurement points the parametric response peaked at around $74 \pm 2°$, clearly identifying the presence of a kissing bond. There is some variation between measurements taken at nominally the same position, but when peak normalised the four different positions show clearly distinct trends. This demonstrates that the method was sensitive to position changes on the order of 1 mm. Therefore some of the error between measurements at the same intended position is likely due to positioning inaccuracies which were approximately ± 0.5 mm.

The largest difference between measurement points in Figure 11 (a) was the drop in amplitude when displacing from the central position. Moving only 2 mm caused a 25% drop in signal. The diameter of the interaction area on the interface at the -3dB limits is estimated to be 21 mm by beam divergence calculations (-3dB was selected rather than -6dB due to the scattering being a product of the square of the input amplitude). In the 2 mm translation roughly 12% of the initial surface area moved outside of the new overlap area. It is possible that a highly CAN active area of the interface was moved outside the interaction region and that the new area was not very active, but the disproportionately large change of 25% means this is unlikely. Another possible explanation is proposed at the end of this section.

Figure 11 (b) also contains some interesting trends. The width of the main peak is much larger at 4 mm displacement and it has a rounded peak. The peak response interaction angle varies by about 4° between the tests and the smaller peak at 100° does not exist other than at 0 mm. Some of these trends are similar to those observed as load was varied in Figure 9, such as peak shifting, but others are quite different, e.g. the large peak width changes. This implies that the shape of the response must be related to more than just average interface loading within the interaction area, indicating that there are other factor(s) causing the variation despite the surfaces being uniformly rough.

The combination of the rapidly changing amplitudes and shapes of the parametric trend therefore probably have a more complex cause than has been discussed above. One explanation is that the overlapping input shear waves constructively produce lines of positive and negative tensile stress on the interface with regions of destructive interference in between. It is these lines where the waves cancel each other that create transmission at the interface when otherwise it might be open due to the tensile forces of the individual beams, thus these lines are the sources of the non-collinearly mixed signal. The lines have a spacing of approximately 1 mm (dependent on interaction angle and frequency ratio) and are at fixed places on the interface when the frequency ratio is one. At other ratios these sampling lines sweep across the interface during the pulse, sweeping faster the further the ratio is away from one. For the case of a 0.9 ratio, as used in this study, the sampling lines will shift back to the starting pattern over the course of 10 cycles of the reference input beam (at 5 MHz in this research). Therefore, the experiment's sensitivity is biased towards the lines of the interface that are sampled when the input pulses are near their maxima due to the peak scattering amplitude being used as the measurement metric. Movement of the sample or change in the interaction angle causes the position of the sampling lines to be altered resulting in the complex parametric-space response that was observed.

5. Conclusions

The non-collinear interaction of two shear waves in a dry, aluminium, compression loaded interface has been studied over a wide range of interaction angles and frequency ratios in the sum-frequency shear-shear mixing regime at around 5 MHz, forming 'fingerprints' of the interface. This sample is intended to simulate an acoustically simple case of a kissing bond to allow the fundamentals of a non-collinear approach to detecting more realistic kissing bonds to be developed. The kissing interface sample displayed nonlinear scattering fingerprints very different from reference solid sample, producing signal at interaction angles between 60° and 120°. At all points in the loading range investigated a characteristic shape was produced, peaking at around 75°. This fingerprint was similar to that predicted by Blanloeuil's FE modelling (13) except for the secondary peaks in the 100° to 120° region in some cases. These peaks were most prominent at higher compressive loads and their cause is unclear. Frequency ratio was not studied in detail in this work as the initial fingerprints had few apparent features in this dimension.

It has been shown that mixing behaviour away from the peak conditions may contain useful information about the interface; e.g. the trends at around the 100° region relating to the interface loading. The interaction angle of peak mixing may be another indicator of interface loading. In this study the peak amplitude correlated well with the interface loading but this trend is not expected to continue at higher contact pressures/lower acoustic pressures, as the interface becomes too highly loaded to be separated by the acoustic waves. There is potential benefit to measuring multiple fingerprint features related to the same interface/material parameter as it would improve the robustness of the method. When different regions of the interface were probed the parameter space changed in ways that did not match with the changes observed due to varied loading. Therefore, further testing of different samples and parts of their interfaces is required to understand the general parametric behaviour of kissing interfaces. It is hypothesised that the position sensitivity is partly due to the non-collinear method only sampling the regions of the interface where the component of stress normal to the interface of the input beams cancel, forming an array of sampling lines. Further testing of a smoother interface in terms of position sensitivity would be of interest in relation to this phenomenon as it would be expected to have properties that vary less spatially. It would also be of interest to test kissing interfaces at higher mechanical compressive loading to investigate the point at which the loading becomes too great for the acoustic waves to separate the surfaces.

The secondary peaks in the interface fingerprints were not predicted by the FE modelling or observed in the solid sample. The precise nature of their source is not known but could be linked to the sampling lines theory mentioned in the previous paragraph. It might be that particular interaction angles sampled the interface at more active regions creating the peaks in response, in a similar way to how the peaks changed when the sample was moved. At low loads the interface had a smoother parametric response. Combining this fact with the sampling theory suggests that the interface has a more uniform contact profile at low loads. Another possible explanation relating to the load based behaviour is that at low loads the interfaces meet more unevenly and the increased deviation in contact angle from the macroscopic surface normal causes a smoothing of the response due to a wider distribution of interaction angles experienced at the microscopic level. This concept alone does not explain the existence of secondary peaks at higher loads however so perhaps it is a combination of effects. These behaviours indicate that the system is highly complex, probably requiring more advanced models and further experimentation to fully understand the impact of kissing bond parameters on their fingerprints.

In the future use of focusing on input beams would allow interaction regions with far fewer overlapping wavefronts to be made. This would probe the interface in greater detail and might confirm if the position sensitivity trends observed with larger interaction areas were a result of interface properties varying on a wavelength scale. If using unfocused beams sweeping the interaction nodes along the interface, perhaps by altering the phase of the beams, and summing the responses together might be a route to measuring a more averaged scattering value for the interaction area. Alternatively frequency ratio ratios further from one with longer pulses could achieve a similar level of sampling coverage. This could be useful if a faster measurement is required than scanning a focus across the whole area and would also ensure that no parts of the interface are unsampled.

In this work there was only one interface at a known depth, in this case a non-collinear c-scan could have been conducted by moving the input transducers and array along the sample. If the defect is at an unknown depth the technique could be easily extended to 3D by sweeping the depth of the interaction volume. The fingerprint at each location might then be analysed to identify the properties of the sample within the interaction volume, allowing 3D positional detection of kissing bonds.

6. Acknowledgments

This work was supported by the Engineering and Physical Sciences Research Council through the EPSRC Centre for Doctoral Training in Advanced Composites for Innovation and Science [grant number EP/G036772/1].

7. References

[1] C. Brotherhood, B. Drinkwater, S. Dixon, The detectability of kissing bonds in adhesive joints using ultrasonic techniques, Ultrasonics 41 (7) (2003) 521–529.

[2] K. Vine, P. Cawley, A. Kinloch, The correlation of non-destructive measurements and toughness changes in adhesive joints during environmental attack, The Journal of Adhesion 77 (2) (2001) 125–161.

[3] I. Y. Solodov, Ultrasonics of non-linear contacts: propagation, reflection and nde-applications, Ultrasonics 36 (1-5) (1998) 383–390.

[4] B. Drinkwater, R. Dwyer-Joyce, P. Cawley, A study of the interaction between ultrasound and a partially contacting solid–solid interface, in: Proceedings of the Royal Society of London A: Mathematical, Physical and Engineering Sciences, Vol. 452, The Royal Society, 1996, pp. 2613–2628.

[5] P. B. Nagy, Ultrasonic detection of kissing bonds at adhesive interfaces, Journal of Adhesion Science and Technology 5 (8) (1991) 619–630.

[6] J. F. Blackburn, M. G. Cain, Nonlinear piezoelectric resonance: A theoretically rigorous approach to constant i- v measurements, Journal of applied physics 100 (11) (2006) 114101.

[7] K. Naugolnykh, L. Ostrovsky, Nonlinear wave processes in acoustics, Cambridge University Press, 1998.

[8] G. L. Jones, D. R. Kobett, Interaction of elastic waves in an isotropic solid, The Journal of the Acoustical society of America 35 (1) (1963) 5–10.

[9] L. H. Taylor, F. R. Rollins Jr, Ultrasonic study of three-phonon interactions. i. theory, Physical Review 136 (3A) (1964) A591.

[10] F. R. Rollins Jr, L. H. Taylor, P. H. Todd Jr, Ultrasonic study of three-phonon interactions. ii. experimental results, Physical Review 136 (3A) (1964) A597.

[11] L. D. Landau, E. M. Lifshitz, Course of Theoretical Physics Vol 7: Theory and Elasticity, Pergamon Press, 1959.

[12] P. Blanloeuil, A. Meziane, A. N. Norris, M. Renier, M. Veidt, Numerical computation of the nonlinear far field of ultrasonic waves scattered by closed cracks of various orientations, in: EWSHM-7th European Workshop on Structural Health Monitoring, 2014.

[13] P. Blanloeuil, A. Meziane, C. Bacon, 2d finite element modeling of the non-collinear mixing method for detection and characterization of closed cracks, NDT & E International 76 (2015) 43–51.

[14] A. Demčenko, V. Koissin, V. Korneev, Noncollinear wave mixing for measurement of dynamic processes in polymers: Physical ageing in thermoplastics and epoxy cure, Ultrasonics 54 (2) (2014) 684–693.

[15] A. J. Croxford, P. D. Wilcox, B. W. Drinkwater, P. B. Nagy, The use of non-collinear mixing for nonlinear ultrasonic detection of plasticity and fatigue, The Journal of the Acoustical Society of America 126 (5) (2009) EL117–EL122.

[16] M. McGovern, W. Buttlar, H. Reis, Characterisation of oxidative ageing in asphalt concrete using a non-collinear ultrasonic wave mixing approach, Insight-Non-Destructive Testing and Condition Monitoring 56 (7) (2014) 367–374.

[17] A. Demčenko, L. Mainini, V. Korneev, A study of the noncollinear ultrasonic-wave-mixing technique under imperfect resonance conditions, Ultrasonics 57 (2015) 179–189.

[18] Z. Zhang, P. B. Nagy, W. Hassan, Analytical and numerical modeling of

non-collinear shear wave mixing at an imperfect interface, Ultrasonics 65 (2016) 165–176.

[19] P. Blanloeuil, A. Meziane, C. Bacon, Numerical study of nonlinear interaction between a crack and elastic waves under an oblique incidence, Wave Motion 51 (3) (2014) 425–437.

[20] J.-Y. Kim, L. J. Jacobs, J. Qu, J. W. Littles, Experimental characterization of fatigue damage in a nickel-base superalloy using nonlinear ultrasonic waves, The Journal of the Acoustical Society of America 120 (3) (2006) 1266–1273.

[21] G. Tang, M. Liu, L. J. Jacobs, J. Qu, Detecting localized plastic strain by a scanning collinear wave mixing method, Journal of Nondestructive Evaluation 33 (2) (2014) 196–204.

[22] Z. Zhang, P. B. Nagy, W. Hassan, Enhanced nonlinear inspection of diffusion bonded interfaces using reflected non-collinear ultrasonic wave mixing, in: AIP Conference Proceedings, Vol. 1706, AIP Publishing, 2016, p. 020023.

[23] W. Wasserbäch, Third-order constants of a cubic quasi-isotropic solid, physica status solidi (b) 159 (2) (1990) 689–697.

[24] V. A. Lubarda, New estimates of the third-order elastic constants for isotropic aggregates of cubic crystals, Journal of the Mechanics and Physics of Solids 45 (4) (1997) 471–490.

[25] J. Krautkrämer, H. Krautkrämer, Ultrasonic testing of materials.

[26] S. Hirose, 2-d scattering by a crack with contact-boundary conditions, Wave Motion 19 (1) (1994) 37–49.

[27] L. Baillet, T. Sassi, Mixed finite element formulation in large deformation frictional contact problem, Revue Européenne des Eléments 14 (2-3) (2005) 287–304.

[28] L. Baillet, T. Sassi, Mixed finite element methods for the signorini problem with friction, Numerical Methods for Partial Differential Equations 22 (6) (2006) 1489–1508.

[29] L. Baillet, T. Sassi, Simulations numériques de différentes méthodes d'éléments finis pour les problèmes de contact avec frottement, Comptes Rendus Mécanique 331 (11) (2003) 789–796.

[30] N. J. Carpenter, R. L. Taylor, M. G. Katona, Lagrange constraints for transient finite element surface contact, International journal for numerical methods in engineering 32 (1) (1991) 103–128.

[31] P. G. Ciarlet, The finite element method for elliptic problems, Elsevier, 1978.